Chapter 5

The Io footprint tail emissions

5.1 Foreword

In the first steps of this work, we adressed basic but essential questions: "What does the Io footprint look like?" and "Where is the Io footprint?". We have seen that the systematic study of the footprint morphology and position lead us to very interesting conclusions. They forced us to discard some early oversimplified ideas and to propose a new interpretation of the footprint multiplicity.

So far, we mainly focused on the spots. Here we concentrate on the tail emission that appears downstream from the spots. The construction of an accurate Io reference oval proves to be extremely useful in the present study since it helps characterizing the tail emission as a function of the distance from the main spot. The Io footprint tail has been detected as early as the UV spots (*Prangé et al.*, 1996), but has not been studied as extensively as the spots. *Prangé et al.* (1998) called it the Io oval and claimed it could take place along a complete contour. However, subsequent images obtained with the much more accurate and sensitive STIS instrument did not show any complete oval, but instead a downstream tail extending downward to more then 100° (*Clarke et al.*, 2002). The term "Io oval" has also been used to designate the locus of all possible Io footprint locations in a reference frame fixed with System III (e.g. *Grodent et al.*, 2003a). As shown above, we now prefer to use "Io reference contour" (or simply "Io contour") to designate this footpath (*Grodent et al.*, 2008a; *Bonfond et al.*, 2009), since it does not form a closed pattern around the pole.

Clarke et al. (2002) claimed that this tail emission cannot be caused by an afterglow persisting after the cessation of particle precipitation, because the H and

H_2 excited upper states decay in a fraction of a second[1]. Hence, they concluded that the UV tail was continuously generated by precipitating charged particles.

The STIS instrument does not only take sharp UV images, it is also and above all a powerful spectrograph. FUV spectra can provide useful information on the amount of absorbing particles along the line of sight. On some STIS FUV spectra of the Jovian aurorae, the slit intercepted the Io footprint main spot or its tail (Figure 5.1). On these spectra, H_2 emissions below 1350 Åare attenuated by the methane while emissions above this threshold are not. The usual parameter to characterize this absorption is the UV color ratio, defined as:

$$CR = \frac{I_{(1550-1620)}}{I_{(1230-1300)}}$$

that is the ratio of the total emission in the wavelength range from 1550 to 1620 Åover the total emission in the wavelength range from 1230 to 1300 Å(*Gérard et al.*, 2002). *Gérard et al.* (2002) measured the color ratio as a function of the distance from the main spot and showed that it does not significantly vary (Figure 5.2). They thus concluded that the brightness decrease along the trail was essentially linked to a decrease of the energy flux rather than to a decrease of the incoming electron energy.

Moreover, with the use of appropriate models and hypotheses, the color ratio can also provide estimates of the precipitating electron energy. Among this set of hypotheses, the choice of a neutral atmosphere model is an important one. *Gérard et al.* (2002) used the North Equatorial Belt (NEB) model from *Gladstone et al.* (1996) adjusted to the gravity acceleration at a latitude of 60°. Another necessary assumption is the vertical distribution of methane in the atmosphere. This distribution is based on infrared spectral measurements in the auroral region obtained with the IRIS instrument on board Voyager 1(*Drossart et al.*, 1993). It also relies on a one-dimensional diffusion equation and on an eddy-diffusion coefficient at the homopause set to 1.4×10^6 cm^{2}s^{-1}. These atmospheric parameters being set, the energy deposition model described by *Grodent et al.* (2001) was used to compute the color ratio as a function of the electron energy, assuming a Maxwellian energy distribution. It should be stated that, contrary to the examples shown in *Grodent et al.* (2001), the thermal structure was not allowed to adjust to the thermal bal-

---

[1]At the exception of one metastable excited state, which have an expected lifetime of seconds, too short anyway to explain the tail.
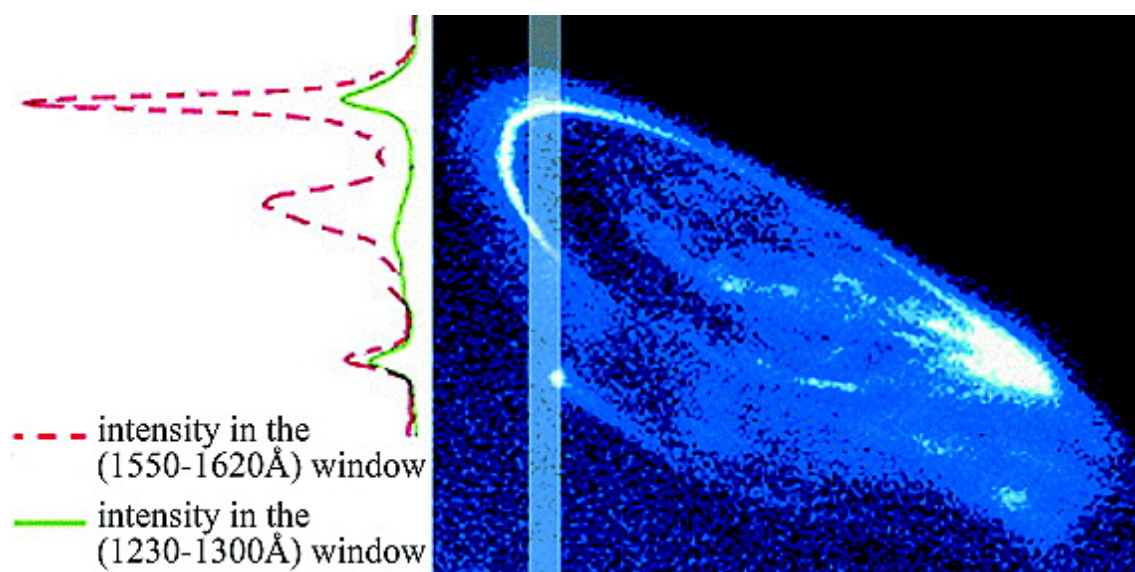
Figure 5.1: The image shows the location of the STIS spectral slit on an image obtained on 22 February 2000, 12 minutes before the spectrum acquisition. The two curves on the left are the intensities along the slit for the two spectral windows of the color ratio. The short wavelength window (in solid green line) is subject to methane absorption while the long wavelength one (in dashed red line) is not. (from *Gérard et al.* (2002))
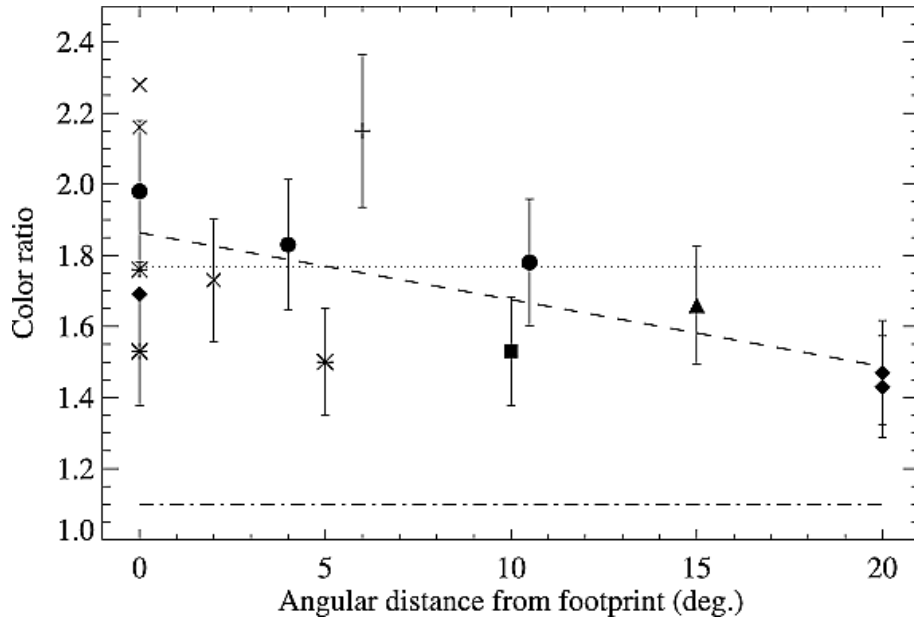
Figure 5.2: Variation of the color ratio observed along the Io trailing tail as a function of the angular distance from the footprint. Identical symbols are used for measurements obtained within one HST orbit. The closed symbols (circle, diamond, square, triangle) correspond to north data, the other symbols (*, +, X) to the south. The dashed line is the linear regression fitted to the north data and the dotted line is the mean color ratio. The dot-dashed horizontal line indicates the color ratio with no hydrocarbon absorption. (adapted from *Gérard et al.* (2002))

ance. In the frame of all these assumptions and models, the energies deduced from color ratio measurements range from 41 to 69 keV and thus a typical precipitating electrons energy in the Io footprint was estimated around 55 keV.

For the sake of completeness, it should be noted that the presence of a footprint tail is not restricted to the case of Io. *Grodent et al.* (2005a) detected a faint (~ 7 kR) tail extending downstream of the Europa spot over ~ 5000 km. Interestingly, these authors noted that the tail was observed when Europa was between 65° and 115° System III longitude, i.e. when Europa is close to the plasma sheet. This could possibly correspond to a suggestion made by *Kivelson et al.* (1999) stating that a plasma plume would only be produced in the wake of Europa when it crosses the current sheet.

Back to Io, we will see in the next section that the longitudinal extent of the tail emission and its separation from the non-Io auroral emissions makes it possible to measure their characteristics with unprecedented accuracy. Most of the material

presented in the following section has been published by B. Bonfond, D. Grodent, J.-C. Gérard, A. Radioti, P.A. Delamere, V. Dols and J.T. Clarke under the title: *The Io UV footprint: Location, inter-spot distances and tail vertical extent* in Journal of Geophysical Research - Space Science (*Bonfond et al.*, 2009).

5.2   Introduction

There are currently few models addressing the tail electrodynamics and all of them assume steady state conditions. They also assume that the tail is the auroral signature of the horizontal divergence of the current crossing the Io plasma wake. This current is needed to reaccelerate the flux tubes, slowed through mass loading by Iogenic plasma, to almost full corotation. *Hill and Vasyliūnas* (2002) applied the same approach as the one proposed for the unipolar inductor model. The Jovian Pedersen conductivity limits the current in the loop connecting the plasma wake of Io and the Jovian ionosphere. Finite ionospheric conductivity thus impedes the return to corotation of the plasma behind Io. *Delamere et al.* (2003) computed the momentum transfer between the plasma in the torus and the plasma slowed by its interaction with Io's atmosphere. After this momentum transfer, they calculated a residual potential drop across the Io flux tube of $\sim$70 kV. They note that if the auroral electrons had to be accelerated by a static potential structure parallel to the field line to the $\sim$55 keV proposed by *Gérard et al.* (2002), then most of the $\sim$70 kV cross-flux tube potential drop available has to be used for this acceleration. They concluded that the corresponding horizontal electric field in Jupiter's ionosphere is thus small and that the Pedersen conductivity is not relevant. Contrary to Hill and Vasyliunas, they concluded that the plasma in the wake of Io is highly decoupled from the Jovian ionosphere. *Ergun et al.* (2009) used the Hill and Vasyliunas approach but added an equation describing the quasi-static potential drop along the magnetic field lines, using a current-voltage relation derived by *Knight* (1973). The Knight current-voltage relation is modified in the model of *Ergun et al.* (2009) to take into account the low plasma density at the foot of the flux tube that limits the parallel (field aligned) current. *Ergun et al.* (2009) computed self-consistently a precipitated electron energy flux of $\sim$1 mW/m^2 compatible with the UV observations, a tail extension comparable to the one deduced by Hill and Vasyliunas (see Section 5.4.2), and a precipitated electron energy of $\sim$1 keV , much smaller than the $\sim$55 keV estimate of *Gérard et al.* (2002).

Some images from the large HST database used for this work show the Io tail emission in such a configuration that its vertical profile can be directly measured. The position of the extracted profiles relative to the main spot was deduced using our new IFP reference contour. We present new measurements describing how the brightness, the peak altitude and the vertical distribution of the tail emission evolve with the distance from the main spot. We also use a Monte Carlo model of the energy degradation of the auroral electrons precipitating into a theoretical Jovian atmosphere in order to compute the UV emission rates from excited H_2 and H. By comparing the simulated emission rates and profiles with the observed ones we deduce the energy distribution of the precipitated electron flux. Consequently, the brightness profiles provide information on the precipitated electrons energies. This technique is therefore independent of the spectral color ratio method. Additionally, this deduced energy distribution gives insight into the physical process accelerating the electrons that we compare with the processes proposed in the models explaining the IFP tail, described earlier in this introduction.

5.3   Peak altitude and vertical profiles

On several ACS images from the 10862 observation campaign, we can clearly see the Io footprint, or at least its trailing tail, lying right above the limb (Figure 5.3). Consequently, we consider here a selection of images where the tail appears crossing the limb plane (Figure 5.4). These images originate from 10 different HST orbits. For this considered observation campaign, a typical orbit was made of 5 consecutive 100-second F125LP images followed by 9 100-second F115LP images and then another 5 100-second F125LP images. For each orbit, the 19 original images are assembled into 7 sets of three images acquired with the same filter (two images are thus used twice) in order to increase the signal to noise ratio while keeping the same integrated exposure time for each set. The first set is the sum of the first three F125LP images, the second is the sum of the 3rd, the 4th and the 5th F125LP images - the image number three is thus used twice. The next three sets sum groups of three images out of the 9 consecutive F115LP images. The last two sets are made of the remaining F125LP images and are respectively formed by the groups from the 15th to the 17th image and by the group from the 17th to the 19th image. Consequently, the 17th image is also used twice. The following data reduction steps are performed on the summed images (7 per orbit). We developed
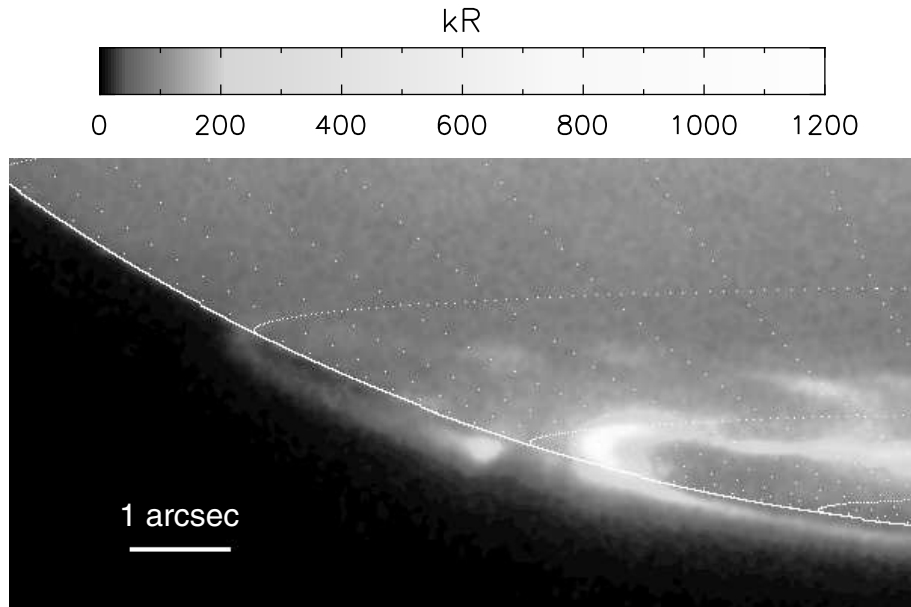
Figure 5.3: Example of Io footprint tail seen right above the limb plane in the southern hemisphere. The reference ellipsoid, where the 0 km altitude is set, has an equatorial radius of 71492 km and a polar radius of 66854 km. Parallel and meridian lines are drawn every 10°. (from *Bonfond et al.*, 2009)

a semi-automatic method to perform radial scans of the planetary limb every 0.1° in a manually selected sector. The routine measures the altitude of the emission peak as a function of the rotation angle, smooths out the resulting curve with a median filter and identifies the maximum altitude (Figure 5.6). If the precipitating particle mean energy is constant along the tail, then the emission peak appearing the furthest from the planetary edge lies in the limb plane. Additionally, the radial profile extracted at this location is assumed to reflect the actual vertical extent of the emission.

Non-auroral planetary disk emissions also contribute to the low altitude part of the observed profiles. Consequently, we built an empirical disk vertical profile extrapolated from profiles extracted at lower latitudes for each image. When we analyze the disk emission, we notice that on the sunlit side of the planet, for a given altitude, the intensity of the disk emission is not evolving significantly as a function of the rotation angle. Consequently, when the tail emission stands over the sunlit limb, the empirical disk profile is formed by the average of the profiles extracted a
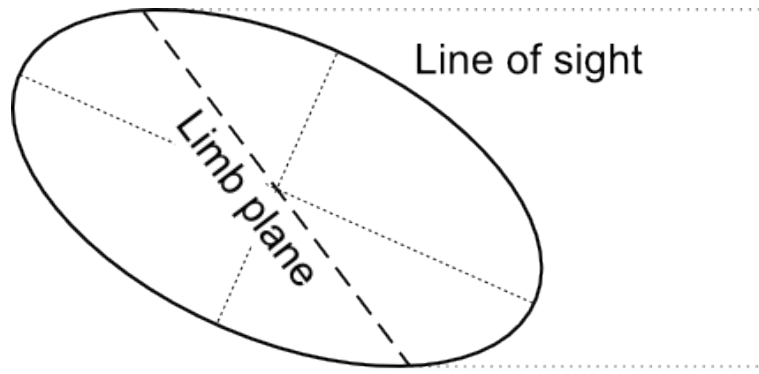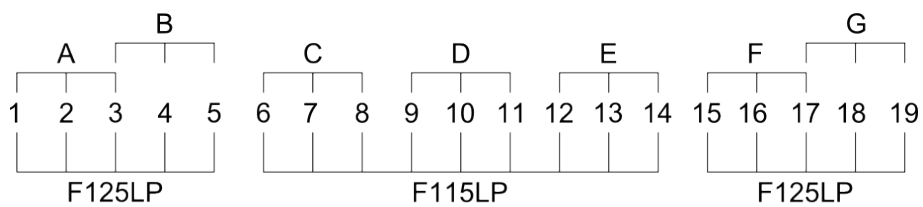
Figure 5.4: Illustration of the limb plane.

Figure 5.5: Schematic of the image regrouping used in this study. The purpose is to increase the signal-to-noise ratio by summing consecutive images acquired with the same filter while keeping the same total exposure time for each set. Images number 3 and 17 are thus used twice.
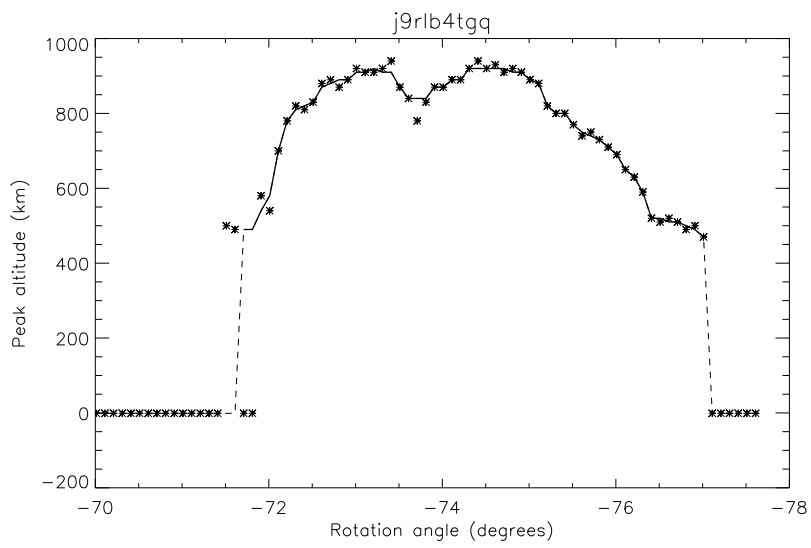
Figure 5.6: Example of the evolution of the Io tail peak altitude as a function of the rotation angle. We then applied a median filter (solid line) and identified the angles and the profile associated with the maximum altitude, which is around 900 km. In the example shown here, the gap in the middle of this profile is probably not significant.

few degrees equatorward from the auroral emissions. On the terminator side of the planet and for a given altitude, we note that the disk emission varies linearly with the rotation angle. Therefore in this case, for a given altitude level, the empirical disk intensity is interpolated from disk profile intensities measured a few tenths of degree equatorward from the tail. We remove this disk emission profile from the total profile in order to isolate the auroral emission. Then we fit the extracted vertical profiles with a Chapman profile of the form :

$$f(x) = C \exp\left(1 - \left(\frac{Z - Z_0}{H} \right) - \exp\left(-\frac{Z - Z_0}{H} \right) \right) \tag{5.1}$$

where C is a constant, Z is the altitude in km, Z_0 is the altitude of the peak in km and H is the scale height in km. The scale height of these emissions lies around 430 km $\pm$ 70 km and does not depend either on the filter nor on the distance from the main spot.

The mean altitude of the emission peak we derive from the profiles is 900 km $\pm$125km. Note that the standard deviation is fairly close to 120 km, which is the typical distance subtended by one pixel on Jupiter. This indicates that the variability due to measurement uncertainty provides an upper limit to the real, intrinsic fluctuations. Figure 5.7 shows the variation of the peak altitude as a function of the longitudinal distance from the Io footprint main spot according to the reference contour described above. The distances are expressed in kilometers along the reference contour to avoid complications owing to the contour geometry. From the length of the reference contours, 2000 km roughly corresponds to $\sim 4°$ in the equatorial plane. Consequently, the furthest points on this plot are approximately 60° away from the main spot. The further the profile stands from the main spot, the higher is the altitude of the brightness peak. However, the correlation coefficient between the altitude and the distance is only 0.09 and is not significantly different from 0 for a confidence interval of 99%. This result justifies *a posteriori* our initial assumption of the constant altitude of the auroral curtain.

5.4   Estimate of the energy distribution

The emission peak altitude provides an estimate of the precipitating particle energy and it puts a strong constraint on the electron acceleration mechanism. Additionally, the emission profile reflects the shape of the energy spectrum. We selected a
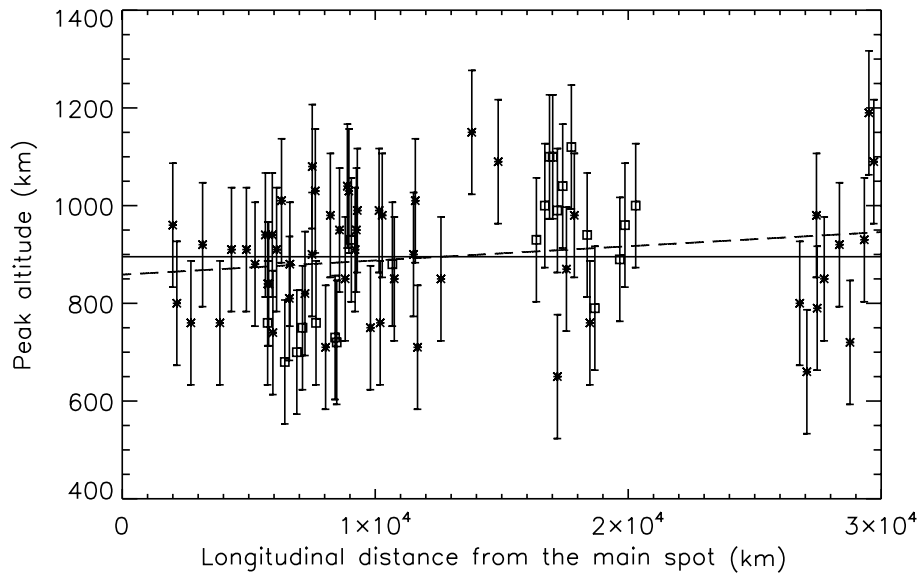
Figure 5.7: Altitude of the peak of the brightness profiles as a function of the distance of this profile from the IFP main spot location as described by our new reference contours. The stars and squares are for points in the northern or the southern hemisphere respectively. The mean altitude is 900km and the increase of the peak altitude is not statistically significant. This indicates that the precipitating electron energy is relatively constant with the distance to the main spot. (from *Bonfond et al.*, 2009)

sub-set of images coming from two consecutive HST orbits acquired on 24/02/2007 in the southern hemisphere to build a typical vertical profile of the tail. This set of 38 images has been chosen because the curtain is quasi-perpendicular to the observer and because auroral diffuse emissions do not contaminate the lower altitude part of the profile. We sum these 38 profiles to generate a typical observed profile with a signal to noise ratio as large as possible ($\frac{S}{N} \simeq 12$ in lieu of ~ 2 for single images) and we compare it to different theoretical emission profiles (Figure 5.8). Spectral measurements showed that hydrocarbon absorption of the IFP FUV emissions was measurable but weak (*Gérard et al.*, 2002). However, we have very little observational information on the methane vertical distribution in the polar regions. Consequently, we consider that hydrocarbon absorption does not significantly affect the shape of the emission vertical profile.

The numerical model used to calculate electron transport in planetary atmospheres has been described in detail by *Shematovich et al.* (2008). The incident electrons lose their excess kinetic energy in elastic, inelastic and ionization collisions with the ambient atmospheric gas consisting of H_2, He, and H. If the collision produces ionization, a secondary electron is created and is randomly assigned an isotropically distributed pitch angle and an energy in accordance with the procedure given by *Garvey and Green* (1976), *Jackman et al.* (1977) and *Garvey et al.* (1977). The cross sections and scattering angles used to calculate the energy loss associated with elastic and inelastic collisions of electrons with H_2, He, and H were taken for H_2 from the AMDIS database (https://dbshino.nfs.ac.jp) and *Shyn and Sharp* (1981); for He and H from the NIST database (http://physics.nist.gov/PhysRefData/Ionization/) and *Jackman et al.* (1977), *Dalgarno et al.* (1999). Their transport is described by the kinetic Boltzmann equation. The Direct Simulation Monte Carlo (DSMC) method is used to solve atmospheric kinetic systems in the stochastic approximation (see *Shematovich et al.*, 2008 and references therein). The lower boundary is set at an altitude 0.25 μbar and the upper boundary is fixed at 6.5×10^{-11} μbar where the atmospheric gas flow is practically collisionless. The region of the atmosphere under study is divided into 49 vertical cells uniformly distributed on a logarithmic pressure scale. The evolution of the system of modeled particles due to collisional processes and particle transport is calculated from the initial to the steady state. The pressure-altitude relationship from *Grodent et al.* (2001) is adopted because it is the most realistic auroral atmosphere available. For a given initial mono-energetic beam, the model provides a vertical emission profile assuming an isotropic pitch

angle distribution at the top of the atmosphere.

If we consider a mono-energetic distribution, the curve that best fits the observations has a typical energy of 2 keV (Table 5.1). However, even after taking the point spread function (PSF) of the ACS camera into account, its vertical width is too small to reasonably reproduce the observations. Because of the curvature of the planet, an extended emission region leads to an apparent broadening of the emission profile. A simulation of the emission integration along the line of sight shows that the size of the emission region should be 20 times larger than the vertical scale height to generate significant effects. In our case, we determine that the curtain latitudinal width corresponds to the projected diameter of Io and lies between 100 and 200 km, i.e. only 0.25 to 0.5 times the observed scale height ($\sim$400 km). Consequently, we may conclude that the width of the vertical emission profiles is due to a broad distribution in the energy of the precipitating electrons. We tested three different energy distributions in order to obtain information on the shape of the particle energy spectrum: a Maxwellian distribution

$$I = CE \exp(\frac{-E}{E_0}) \tag{5.2}$$

a power law distribution

$$I = CE^{-\gamma} \tag{5.3}$$

and a kappa distribution

$$I = CE(E + E_0\kappa)^{-1-\kappa} \tag{5.4}$$

where I is the differential intensity in $cm^{-2}s^{-1}sr^{-1}keV^{-1}$, E is the electron energy in keV, C is a constant, E_0 is the characteristic energy in keV, and γ and κ are the spectral indices of the power-law and the kappa distributions, respectively. For each distribution, we divide the energy range between 30 eV and 30 keV into 30 energy bins (uniformly distributed on a logarithmic energy scale) in which we compute the mean energy and the total energy flux[2]. We simulate an emission profile for each energy bin with the Monte Carlo model. Finally we weight the emission profiles with the channel total energy flux and we sum them to generate the emission profile corresponding to the adopted distribution and set of parameters. After smoothing

---

[2]In an energy range from E_1 to E_2, the total energy flux is calculated as:

$$E_t = \int_{E_1}^{E_2} EIdE$$

Distribution	Characteristic energy (E_0)	Spectral index (γ or κ)	Mean energy
Mono-energetic	2 keV (1.3 keV)	-	2 keV (1.3 keV)
Maxwellian	960 eV (540 eV)	-	1.9 keV (1.1 keV)
Kappa	70 eV (75 eV)	2.3 (2.4)	1.1 keV (0.8 keV)
Power-law	-	1.9 (1.8)	-

Table 5.1: Parameters of the best fit curves compared to the summed profile acquired $\sim 20°$ away from the main spot. The numbers between brackets are computed for a profile located approximately $40°$ away from the spot.

the profile with a boxcar function of the size of the PSF, we perform a least squares fit to compute the best parameter set for each energy distribution. The results are given in Table 5.1. Figure 5.9 presents the best fit energy spectra used to compute the corresponding emission profiles. Figure 5.8 shows the best simulated vertical profiles and compares them with the observations. One can note that only the kappa distribution generates a vertical profile compatible with the observations. The profiles that we used for the best fit lie approximately $20°$ away from the main spot. We also perform the same analysis with profiles taken approximately $40°$ away from the main spot (not shown here). Since the brightness is lower and only 19 images are used, the signal to noise ratio is lower but the results are very similar and are presented between brackets in Table 5.1.

5.4.1 Sensitivity tests

One of the main unknowns when we try to deduce the electron energy distribution based on a vertical profile is the pressure-altitude relationship for the atmosphere. We adopted here, as our basic model, an atmosphere model that takes heating due to particle precipitation in account (*Grodent et al.*, 2001). We also performed the same test for two other atmospheric models: the NEB model and an artificially hot atmosphere (designated as 2X hereafter) which is our basic atmosphere where all the altitudes were multiplied by a factor 1.5 and shifted by 80 km (see Figure 5.10).

Whatever the case, the mono-energetic and the Maxwellian distributions are

---

and the mean energy is computed as as the ratio of the energy flux over the particle flux:

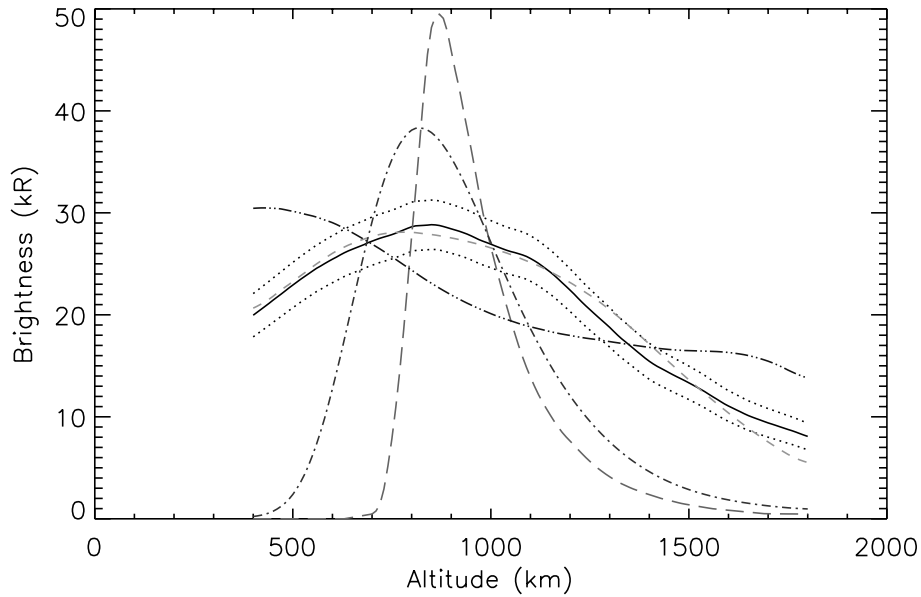$$E_m = \frac{\int_{E_1}^{E_2} EIdE}{\int_{E_1}^{E_2} IdE}$$

Figure 5.8: Observed and simulated vertical emission profiles. The observations and the estimated uncertainties are represented by the solid line surrounded by the dotted lines. The four other lines are the best fit vertical profiles based on the theoretical distributions described in the text. The long dashed line corresponds to the mono-energetic distribution, the small dashed line corresponds to the kappa distribution, the dash-dotted line corresponds to the Maxwellian distribution and the dash-dot-dot-dotted line corresponds to the power-law distribution. One can see that only the kappa distribution provides a reasonable fit of the observed curve. (from *Bonfond et al.*, 2009)
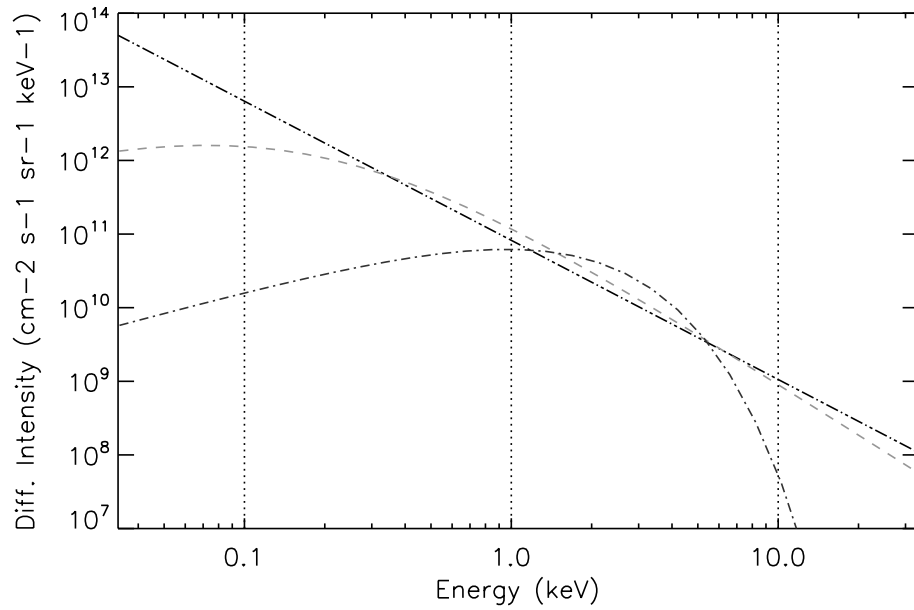
Figure 5.9: Energy spectra computed with the best fit parameters shown in table 5.1. The dashed line represents the kappa distribution, the dash-dotted line represents the Maxwellian distribution and the dash-dot-dot-dotted line represents the power-law distribution. In order to compute the differential intensities, the curtain is assumed to be 200 km wide. (from *Bonfond et al.*, 2009)

NEB Distribution	Characteristic energy (E_0)	Spectral index (γ or κ)	Mean energy
Mono-energetic	552 eV	-	552 eV
Maxwellian	283 eV	-	566 eV
Kappa	5 eV	2.12	177 eV

Table 5.2: Parameters of the best fit curves compared to the summed profile acquired ∼20° away from the main spot, considering the NEB atmosphere model.

2X Distribution	Characteristic energy (E_0)	Spectral index (γ or κ)	Mean energy
Mono-energetic	7.7 keV	-	7.7 keV
Maxwellian	2.7 keV	-	5.4 keV
Kappa	270 eV	2.35	3.6 keV

Table 5.3: Parameters of the best fit curves compared to the summed profile acquired ∼20° away from the main spot, considering the 2X atmosphere model.

always too narrowly peaked to reproduce the observation (Figures 5.11 and 5.12). In the case of the NEB atmosphere, even the kappa distribution cannot reproduce the observed curve. This can be easily explained by the fact that observations show significant emission at altitudes as high as 1500 km and above, while in the NEB model, the atmospheric pressure is already more than one order of magnitude lower than for the basic model. Thus, a very large amount of low energy electrons are required to reproduce the observations, but then the kappa distribution is no longer able to fit the remainder of the curve. Tables 5.2 and 5.3 show that the mean energies vary with a factor of 4 at maximum, if we exclude the kappa results for the NEB test.

Another source of uncertainty comes from the measured altitudes. Therefore, we also performed test fits after shifting the observed curve by ±120 km. The mean energies are modified by a factor of two at most compared to the basic test. Additionally, the mono-energetic and the Maxwellian distributions are unable to reproduce the width of the observed profile, contrary to the kappa distribution. The computed distribution parameters for these two runs are collected in Tables 5.4 and 5.5.
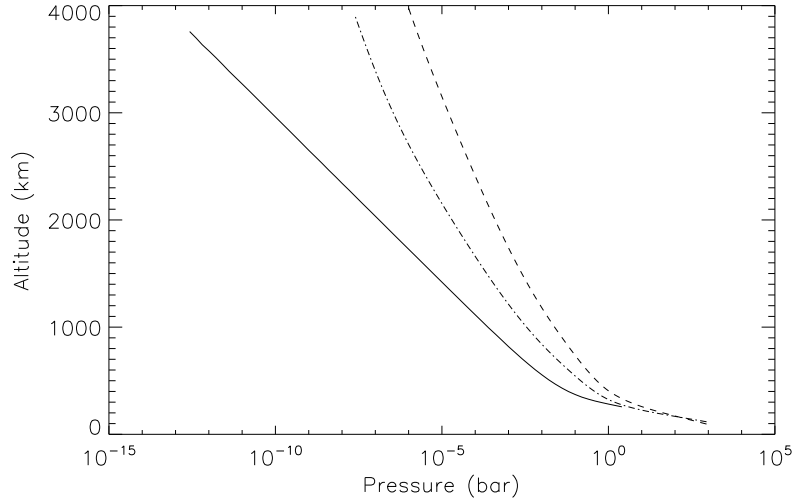
Figure 5.10: Altitude-pressure relationship for the NEB model in solid line, for the *Grodent et al.* (2001) model in dash-dotted line and for the artificially hot 2X model in dashed line.

+120 km Distribution	Characteristic energy (E_0)	Spectral index (γ or κ)	Mean energy
Mono-energetic	1.3 keV	-	1.3 keV
Maxwellian	650 eV	-	1.3 keV
Kappa	62.5 eV	2.4	750 eV

Table 5.4: Parameters of the best fit curves compared to the summed profile acquired $\sim$20° away from the main spot and shifted 120 km upward.

-120 km Distribution	Characteristic energy (E_0)	Spectral index (γ or κ)	Mean energy
Mono-energetic	3.3 keV	-	3.3 keV
Maxwellian	1.5 keV	-	3.0 keV
Kappa	57.5 eV	2.1	2.4 keV

Table 5.5: Parameters of the best fit curves compared to the summed profile acquired $\sim$20° away from the main spot and shifted 120 km downward.
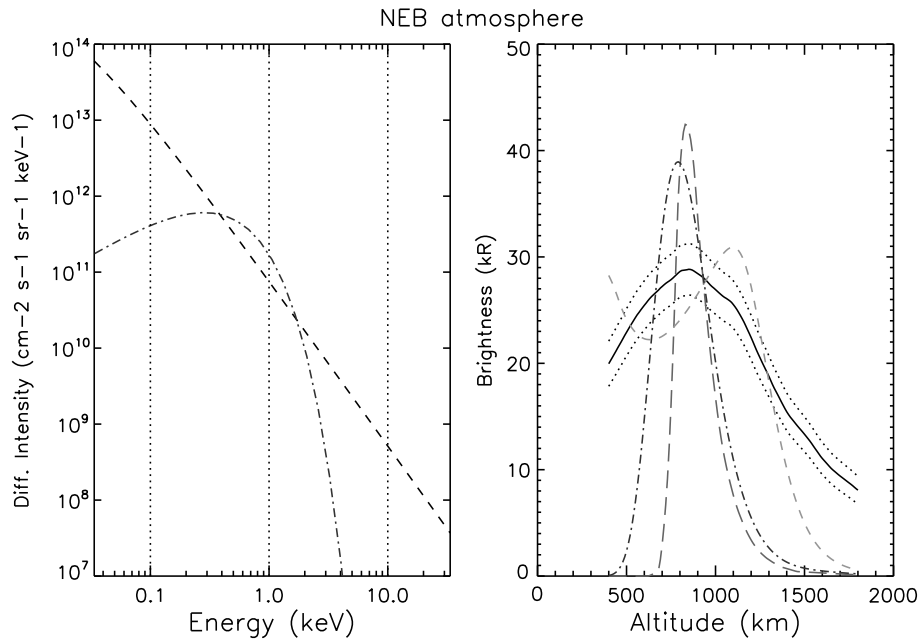
Figure 5.11: (left) Energy spectra computed with the best fit parameters shown in table 5.2. The small dashed line corresponds to the kappa distribution and the dash-dotted line corresponds to the Maxwellian distribution. (right) Observed and simulated vertical emission profiles for the NEB atmosphere. The observations and the estimated uncertainties are represented by the solid line surrounded by the dotted lines. The long dashed line corresponds to the mono-energetic distribution, the small dashed line corresponds to the kappa distribution and the dash-dotted line corresponds to the Maxwellian distribution.
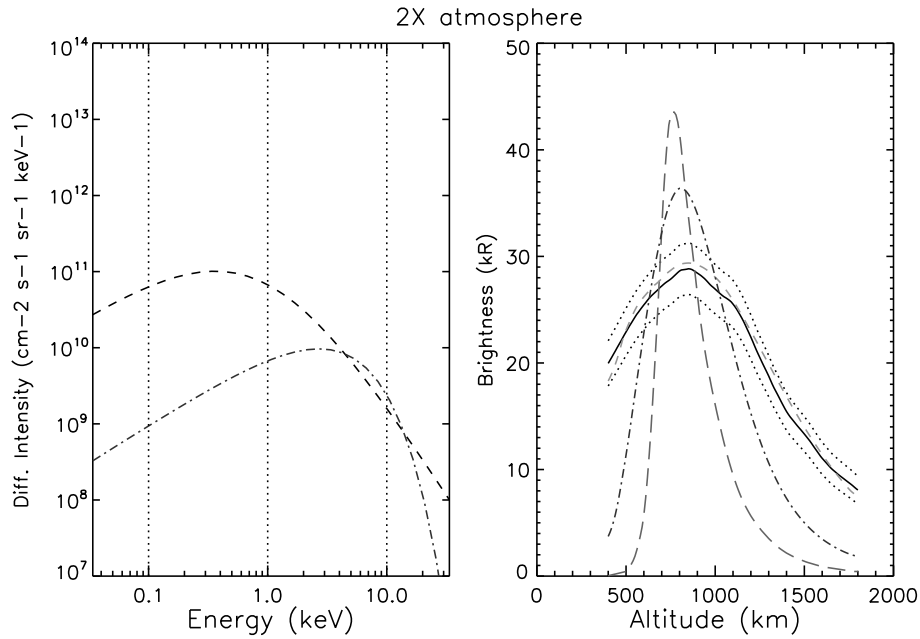
Figure 5.12: (left) Energy spectra computed with the best fit parameters shown in table 5.3. The small dashed line corresponds to the kappa distribution and the dash-dotted line corresponds to the Maxwellian distribution. (right) Observed and simulated vertical emission profiles for the 2X atmosphere. The observations and the estimated uncertainties are represented by the solid line surrounded by the dotted lines. The long dashed line corresponds to the mono-energetic distribution, the small dashed line corresponds to the kappa distribution and the dash-dotted line corresponds to the Maxwellian distribution.
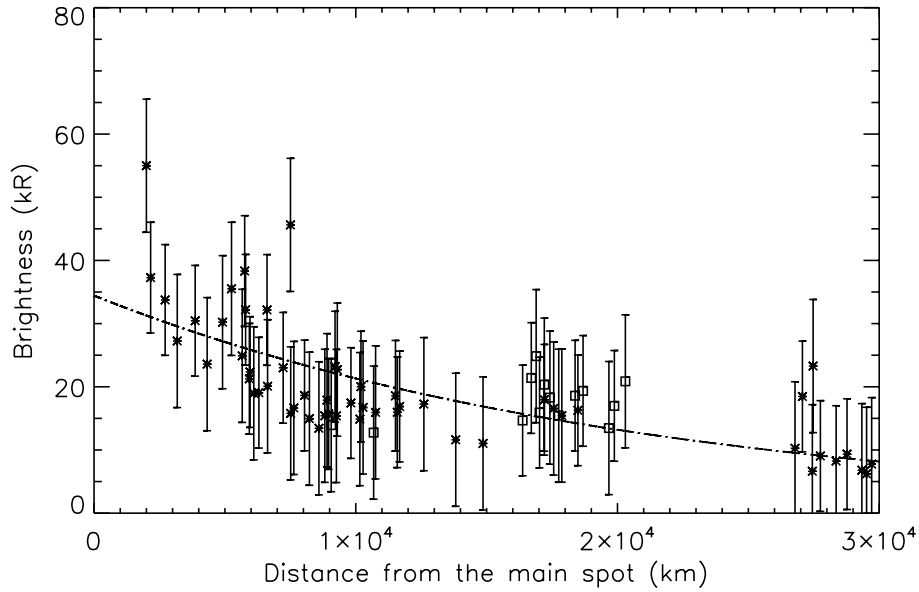
Figure 5.13: Maximum brightness as a function of the distance from the considered cuts to the IFP main spot location as described by our new reference contours. Note that this brightness is measured as seen from HST and does not correspond to the brightness an observer would see, when looking down vertically on the emission point. Northern hemisphere observations are represented by stars while southern hemisphere ones are represented by squares. The dash-dotted line is the least squares best fit with an exponential law. (from *Bonfond et al.*, 2009)

5.4.2 Tail brightness

The extracted vertical profiles also make it possible to measure the tail brightness as a function of the longitude angle between the profile and the main spot. Figure 5.13 shows the evolution of the maximum tail brightness with the distance from the spot. To compare these brightnesses, the tail is considered to be perpendicular to the line of sight. Consequently, the image brightness is corrected for the sine of the angle between the curtain direction and the line of sight. The least-squares fit of the brightness variation with an exponential law has an e-folding length of 21000 km and is shown on the same figure. This value is ~4 times larger than the distance derived by *Hill and Vasyliūnas* (2002). However, their estimate is based on the first 15000 kilometers of the tail while our measurement includes points located twice as far. Considering that the latitudinal width of the tail is equal to Io's diameter as mapped along the field lines, we estimate the energy flux injected into the tail to be between 2 and 20 mW/m^2.

5.5   Discussion

The average altitude at the emission peak derived from vertical profiles is 900 km
± 125 km. This peak altitude is fairly constant with the distance from the main
spot, which indicates that the mean energy of the precipitating electrons is relatively
stable all along the tail. The decrease of the tail brightness shown in Figure 5.13
is most likely attributable to a drop in the particle flux, as suggested by color ratio
measurements (*Gérard et al.*, 2002). However, the color ratio measurements only
extend down to 20° downstream of the main spot while our data span the range
from 4° to 60°. Figure 5.13 shows that the tail brightness appears to decrease faster
close to Io than further downstream. This difference may be partly attributed to a
contamination from emissions coming from secondary spots in the first few thousand
kilometers. Nevertheless, it could also be consistent with models expecting the wake
plasma velocity lag to decrease quickly before reaching an exponential regime. The
injected energy fluxes inferred from the tail brightness lie between 2 and 20 mW/m^2
and are slightly higher than those predicted by *Ergun et al.* (2009). Assuming that
the precipitating electron population is mono-energetic, the energy corresponding to
900 km is 2 keV if we consider the heated atmosphere from *Grodent et al.* (2001). On
the other hand, *Gérard et al.* (2002) concluded that IFP electrons would have a typ-
ical energy of ∼55 keV under the assumption that the methane vertical profile and
the pressure-altitude relationship at the North Equatorial Band (NEB) (*Gladstone
et al.*, 1996) also apply to the polar regions. However, *Grodent et al.* (2001) showed
that the thermal structure of the atmosphere is significantly modified by the auroral
energy input. We note that our mean value is much lower than estimates inferred
from color ratio measurements, but is closer to the energy that electrons would ac-
quire in the 1 kV potential drop computed by *Ergun et al.* (2009). Nevertheless,
the constant 430 km scale height of the vertical emission profiles indicates that the
precipitating electron distributions can be neither mono-energetic nor Maxwellian.
In the Earth's aurora, mono-energetic distributions are usually linked to inverted-
V structures, where the electrons are accelerated by quasi-static potential drops.
Maxwellian distributions are most often associated with isotropically heated popu-
lations. As expected, a power-law overestimates either the low energy part of the
spectrum, if the spectral index is too high, or the high energy part in the opposite
case, but it never produces a peaked curve resembling the observations. In the IFP
tail case, the only distribution that reasonably reproduces the observations is a kappa

distribution with a relatively low characteristic energy. Such broad energy distributions could be related to electron acceleration by inertial Alfvén waves (*Ergun et al.*, 2006; *Swift*, 2007). The inertial Alfvén modes arise when one takes finite electron inertia into account in obtaining the dispersion relation and when the perpendicular wavelength of the Alfvén wave is on the order of the local electron skin depth (*Jones and Su*, 2008). Sensitivity tests performed either for the NEB atmosphere or for an empirical very hot atmosphere showed that the characteristic energies could change by a factor of four at most. However, vertical profiles produced by mono-energetic or Maxwellian distributions would never be as extended as observed, whatever the atmospheric model we use. Similarly, shifting the profile by 120 km up or down to simulate the 1-pixel pointing uncetainty could change the mean energies by a factor of two at most, but the conclusions on the best energy distribution would remain unchanged as well. Consequently, even if the predicted energy flux and the particle mean energy are reasonable, the assumption that electrons are accelerated by a localized static electric field as proposed by *Ergun et al.* (2009) does not seem to be in agreement with the vertical extent of the emission profile. Incidentally, we note that the κ spectral index we infer from our calculations is very similar to the $\kappa = 2.4$ value measured in the plasma torus by Ulysses (*Meyer-Vernet et al.*, 1995). However, an initial kappa population further accelerated through a static electric potential would lack low energy electrons, contradicting our observations.

Even if the definitive explanation is out of the scope of this paper, two possible reasons could be invoked to reconcile the high emission peak altitude and the weak but undeniable methane absorption in FUV spectra. First of all, energies derived from color ratio measurements assume a Maxwellian distribution of the precipitating electrons. We show here that a broader energy spectrum is needed to fit the observations. This implies that part of the impinging electrons can penetrate deep into the atmosphere, while another part will lose most of its energy in the upper atmosphere. Thus the observed absorption could result from the combination of strong absorption of the emissions caused by the more energetic particles and weak or no absorption of the high altitude emissions. The use of an auroral heated atmosphere as proposed by *Grodent et al.* (2001) could also help raise the methane homopause. Moreover, their 1D model only takes the diffusion of atmospheric particles into account, and does not consider 3D convective phenomena. Thus, the second possibility is that vertical winds triggered by auroral precipitation could also transport hydrocarbon molecules from the near homopause region to higher altitudes. The energy input

should be on the order of the total thermal energy in the atmospheric column to generate convection (*Smith*, 1998). At an altitude of 900 km, this thermal energy is equal to ~ 125 J for a 1 m^2 cross section column. Consequently, assuming that tail precipitating energy flux is on the order of $10\,mW/m^2$, approximately 3.5 hours are required to provide this amount of energy. In a reference frame fixed to Jupiter, Io moves by $\sim 100°$ during this time interval. Strictly speaking, this would mean that convection is likely to take place above 900 km, but would be established in the downstream part of the tail only. However several points need to be taken into account that could mitigate this statement and lead to faster and deeper convection. First, we neglected the impact of the spots which are at least 10 times brighter than the tail. Secondly, we did not consider the fact that a point on the reference contour is heated repeatedly for 3.5 hours every Io rotation, i.e. approximately every 13h. Thirdly, we neglected Joule heating associated with Pedersen currents. And finally, it must be noted that the estimator provides the order of magnitude required to establish some convection, but does not replace a dynamic and self consistent 3D analysis of the impact of the IFP on Jupiter's upper atmosphere. Furthermore, a full 3D analysis would also take into account additional energy transport mechanisms such as conduction, horizontal advection and radiation, which may possibly mitigate or suppress the onset of convection. Further studies are needed to determine if and how convection takes place and whether it would originate deep enough to raise the hydrocarbon molecules.

5.6   Conclusions

Owing to its particular geometry and its isolation from any other auroral emissions on Jupiter, the tail vertical profiles provide a unique opportunity to verify that the observed emission profile is exactly in the limb plane. The observed peak altitude is surprisingly high ($\sim$900 km above the limb), which suggests that the involved electrons have a mean energy around 1-2 keV. As shown in the first section of this chapter, color ratio measurements showed that the tail is located approximately at the same altitude as the main spot and the precipitating electron energy was expected to be around 55 keV. Note that these estimates do not assume the same atmosphere model, but sensitivity tests performed with the NEB atmosphere indicate that such a difference in the energies cannot be attributed to the atmosphere model alone. The fact that hydrocarbon absorption was clearly observed was consid-

ered as the evidence that the emission takes place close to the methane homopause. Nevertheless, the estimate of the incoming electron energy rested on a set of hypotheses assumed to be reasonable but poorly constrained by measurements in the polar region. Consequently, the apparent disagreement between the occurrence of methane absorption and the observed tail altitude is an additional evidence that the structure of the atmosphere in the polar regions is still barely understood. The response of the atmosphere to the cyclic but highly localized energy input in the Io footprint would certainly deserve a detailed modelling, which is unfortunately out of the scope of this thesis.

The second surprise arising in this study is the width of the vertical profiles. The shape of the observed vertical emission profiles is too wide to be explained by a mono-energetic distribution of the precipitating electrons. Using the auroral heated atmosphere from *Grodent et al.* (2001), a best fit is obtained for a kappa distribution with a characteristic energy of $\sim$70 eV, a spectral index of 2.3 and a mean energy $\simeq$1 keV. Additionally, the peak altitude and the profile vertical width do not evolve significantly along the tail, while the brightness decreases with distance. Most of the previous interpretations of the tail emission, the most noticeable probably being the ones proposed by *Crary and Bagenal* (1997) and *Delamere et al.* (2003), assumed that the initial Alfvénic interaction would somehow evolve into a stationary process in the downstream direction. Hence, all the models specifically considering the tail generation mechanism assume a stationary regime (*Hill and Vasyliūnas*, 2002; *Delamere et al.*, 2003; *Ergun et al.*, 2009). In these stationary models, it seems natural (but not necessarily mandatory[3]) to attribute the electron acceleration to a static feature, i.e. a static electric field. The fact that our observations cannot be reproduced with mono-energetic or Maxwellian distributions puts this assumption into question. The broad energy spectrum suggests that inertial Alfvén waves accelerate the electrons that cause the tail aurora. One possible way to prove that inertial Alfvén waves are involved could rest on the presence of electron beams in the equatorial plane downstream of Io, showing that electrons are accelerated in both directions. Thus the same electron acceleration process could take place both for the spots and the tail.

After this detour on the spatial structure of the tail emission, the next chapter will come back to the spots and will examine the spatial structure of the spots. The understanding of the 3D extension of the Io footprint emissions is crucial for the

---

[3]Only the *Ergun et al.* (2009) model requires explicitly a static electric field

last step of the work: the study of the Io footprint brightness.